Dalton Transactions

ROYAL SOCIETY OF CHEMISTRY

PAPER

View Article Online
View Journal | View Issue

Check for updates

Cite this: *Dalton Trans.*, 2025, **54**, 15259

Modulating axial anisotropy in tetrahedral Co(II) phosphonate single-ion magnets through N-donor ligands

Ananta Patwal, Rajanikanta Rana, Gopalan Rajaraman* and Ramaswamy Murugavel *

Received 20th June 2025,
Accepted 3rd September 2025

DOI: 10.1039/d5dt01461a

rsc.li/dalton

Mononuclear cobalt(II) phosphonate complexes $[Co(HL)_2(dmpz)_2]$ (**1**), $[Co(HL)_2(imz)_2]$ (**2**) and $[Co(HL)_2(bimz)_2]$ (**3**) (where dmpz = 3,5-dimethylpyrazole, imz = imidazole and bimz = benzimidazole) have been synthesized by reacting cobalt acetate tetrahydrate and the α-hydroxyarylphosphonate $[(2,6\text{-}^{i}Pr_2C_6H_3O)P(O)(OH)(CMe_2(OH))]$ (**H_2L**) with chosen N-donor ligands. Complexes **1–3** have been characterized by various spectroscopic and analytical techniques. Single-crystal X-ray diffraction studies reveal that complexes **1** and **2** exist in tetrahedral geometries with $\{CoN_2O_2\}$ as the core coordination unit, while complex **3** shows a vacant trigonal bipyramidal geometry with one exceptionally long Co–O bond. Magnetic susceptibility measurements reveal the existence of high-spin cobalt(II) centres with zero-field splitting parameters (D) of –18.9 cm^{-1} (for **1**), –13.7 cm^{-1} (for **2**), and 22.3 cm^{-1} (for **3**) with E/D values of 0.02, 0.11 and 0.25, respectively. *Ab initio* CASSCF/NEVPT2 calculations and X-band EPR spectroscopic analysis further confirm the observed trend, revealing a switch in the sign of the zero-field splitting parameter (D) from negative in complexes **1** and **2** to positive in complex **3**. Investigation of the dynamic magnetic behaviour of these complexes shows field-induced slow relaxation of magnetization under an applied dc field with energy barriers for reversal of magnetization (U_{eff}) of 31.9 K (**1**), 32.5 K (**2**), and 26.2 K (**3**), indicating SIM behaviour. *Ab initio* CASSCF/NEVPT2 calculations performed on three structurally related Co(II) complexes reveal a switch in the sign of the axial zero-field splitting parameter (D), despite their comparable chemical environments. A detailed magneto-structural correlation study identifies the combined influence of conventional angular distortions from ideal tetrahedral geometry and the Co–O–P bond angle as key determinants, establishing a predictive framework for tuning magnetic anisotropy in cobalt phosph(on)ate-based SIMs.

Introduction

Single-molecule magnets (SMMs) are discrete molecules that exhibit slow relaxation of magnetization due to the presence of an energy barrier for spin reversal—a property that makes them promising candidates for applications in high-density magnetic information storage,[1–4] quantum computing,[5,6] and spintronics.[7–10] Historically, the field of SMMs was dominated by large polynuclear clusters, such as the iconic Mn_{12}-acetate reported in 1993, where the strategy focused on increasing the total ground-state spin S by incorporating multiple magnetic centres.[11,12] This approach was motivated by the direct correlation between the effective energy barrier (U_{eff}) and the spin quantum number, as described by the equations $U_{eff} = DS^2$ for integer S and $U_{eff} = D(S^2 - 1/4)$ for half-integer S, where D is the axial zero-field splitting (ZFS) parameter.[13] However, it soon became clear that increasing S often came at the expense of reducing D, due to their inverse relationship, ultimately limiting the overall barrier height.

This realization shifted the focus of research towards maximizing magnetic anisotropy (D) in mononuclear complexes—ushering in the era of single-ion magnets (SIMs), where a single metal ion is embedded in a ligand field that enhances its magnetic anisotropy.[14–16] By precisely tuning the ligand environment around a single centre, researchers aim to optimize D directly, circumventing the limitations posed by the earlier polynuclear strategy.[17] Among transition metals, cobalt-based SIMs have emerged as top-performing systems due to their strong spin–orbit coupling and highly anisotropic electronic structures, making them ideal candidates for next-generation molecular magnetic materials.[18]

Over the past few years, lanthanide-based SIMs have demonstrated significant advancement, reporting exceptionally high energy barriers.[19–21] Owing to their unquenched

Department of Chemistry, Indian Institute of Technology Bombay, Powai, Mumbai 400 076, India. E-mail: rajaraman@chem.iitb.ac.in, rmv@chem.iitb.ac.in

orbital angular momentum and strong spin-orbit coupling (SOC), lanthanide metal-based SIMs exhibit significant relaxation barriers and high blocking temperatures (T_B).[22,23] However, being rare earth metals, they are expensive, and most of the reported complexes exhibiting high U_{eff} values are not air stable. Later, Long *et al.* reported a low-coordinated high-spin iron(II) complex $[Fe(tpa^{Mes})^-]$,[24] which inspired researchers to explore the role of various transition metal ions in the field of single-ion magnetism.[25–27]

Compared to other transition metal ions, Co(II)-based SIMs show enhanced magnetic properties due to slow magnetic relaxation behaviour originating from the high-spin Co(II) centre with a non-integer ground state. Furthermore, cobalt ions possess significant SOC and Kramers degeneracy-induced ground-state bistability.[28]

Using phosphonic acids[29–35] and α-hydroxyarylphosphonates[36] as precursors, a range of transition metal phosphate compounds has been reported by us and others. Due to the presence of two acidic P–OH protons in phosphonic acids, the reaction with transition metals often results in the formation of dimeric or polymeric complexes.[29–35] By substituting an acidic P–OH group with an alcoholic hydroxyl group, the phosphonic acid moiety can be structurally tailored to promote the formation of monomeric complexes. The magnetic properties of such molecules solely depend on a single metal centre, and zero-field splitting (anisotropy) plays an important role in monomeric complexes. The increase in the Co–Co distance between cobalt centres mitigates magnetic exchange coupling interactions, thus improving the single-molecule magnet (SMM) behaviour.[37]

Ligand design and precise control over geometry play a key role in tuning their magnetic properties. Trigonal prismatic Co(II) complexes, which exhibit near D_3 symmetry in a six-coordinate environment, have gained attention due to their pronounced uniaxial magnetic anisotropy. One such cobalt(II) cage complex with a trigonal prismatic geometry exhibits a high Orbach relaxation barrier of 152 cm^{-1}.[38] Two other similar mononuclear trigonal prismatic Co(II) complexes, [Co(tppm*)][BPh_4]$_2$ and [Co(hpy)][BPh_4]$_2$·3CH_2Cl_2, exhibit dramatically different performance. The former exhibits a U_{eff} value of 192 cm^{-1} and has a nearly ideal trigonal prismatic geometry, whereas [Co(hpy)][BPh_4]$_2$·3CH_2Cl_2 is more distorted, yielding only a value of 20 cm^{-1}, highlighting the sensitivity of relaxation dynamics to geometric precision owing to structural distortion and symmetry breaking.[39,40]

A four-coordinate cobalt(II) complex, [$(HNEt_3)_2$Co(II)$(L)_2$] (**H_2L** = 1,2-bis(methane-sulfonamido)benzene), exhibited SIM behaviour with a spin-reversal barrier of 118 cm^{-1}, while a linear two-coordinate cobalt(II) complex, [Co(C{$SiMe_2ONaph$}$_3$)$_2$], reported by Long and co-workers, demonstrated a significantly higher barrier of 450 cm^{-1}.[41] These low-coordinate Co(II) SIMs are particularly promising due to their pronounced magnetic anisotropy, which stems from strong spin–orbit coupling and ligand field effects. However, despite their excellent magnetic performance, two-coordinate systems typically require cryogenic temperatures to function and are highly sensitive to air and moisture.[42,43] In contrast, four-coordinate complexes, especially those with tetrahedral coordination environments, offer a compelling balance between performance and stability, making them more viable for practical applications.[44,45] In such tetrahedral systems, the zero-field splitting (ZFS) parameter D is often substantial and highly sensitive to deviations from ideal T_d symmetry, which has drawn significant interest in understanding how structural distortions affect magnetic anisotropy.[46–48]

Against this backdrop, tailoring the sign and magnitude of the ZFS parameter D through deliberate structural distortions has emerged as a central strategy for establishing magneto-structural correlations in Co(II)-based SIMs. Among various structural motifs, tetrahedral Co(II) complexes remain some of the most robust and tunable platforms in this context. Prior efforts have employed halide substitution, heavy-atom incorporation, or soft donor ligands to modulate D, often achieving a switch in its sign and magnitude.[49,50] However, there remains a lack of systematic investigations exploring whether subtle, chemically minimal modifications in the ligand backbone alone—without altering the donor type or the coordination number—can exert a comparable influence. This study addresses this gap by examining a family of three structurally analogous ligands: dmpz (3,5-dimethylpyrazole), imz (imidazole) and bimz (benzimidazole). These ligands enable a controlled framework to test the hypothesis: can minor ligand architecture modifications modulate D in both strength and sign? If so, what structural features—such as angular distortions, donor atom orientation, or electronic effects—govern such changes? These questions form the core objectives of this work, aimed at deepening our understanding of how molecular symmetry and ligand design dictate magnetic anisotropy in Co(II)-based SIMs.

Results and discussion

Synthesis of $[Co(HL)_2(dmpz)_2]$ (1), $[Co(HL)_2(imz)_2]$ (2) and $[Co(HL)_2(bimz)_2]$ (3)

The synthetic protocol used for the preparation of **1–3** is outlined in Scheme 1. N-Donor ligands 3,5-dimethylpyrazole (dmpz) or imidazole (imz) were reacted with α-hydroxyarylphosphonate (**H_2L**) and Co(OAc)$_2$·4H_2O in MeOH at room temperature. Slow evaporation of solvent at room temperature yields blue crystals of complexes **1** and **2**. Similarly, the reaction of the **H_2L** ligand and Co(OAc)$_2$·4H_2O with benzimidazole yields a violet precipitate, which was subsequently dissolved in acetonitrile and crystallized to produce violet colour X-ray-quality crystals of complex **3**. All the complexes are stable under ambient conditions.

The Fourier transform infrared (FT-IR) spectra of all the complexes were recorded as KBr-diluted discs. The broad band appearing in the 3395–3100 cm^{-1} range corresponds to the symmetric and asymmetric stretching modes of N–H bonds in the amine derivatives and the un-deprotonated hydroxyl group of the phosphonate ligand. The absence of any peak at 2300 cm^{-1} indicates the deprotonation of the P–OH group of

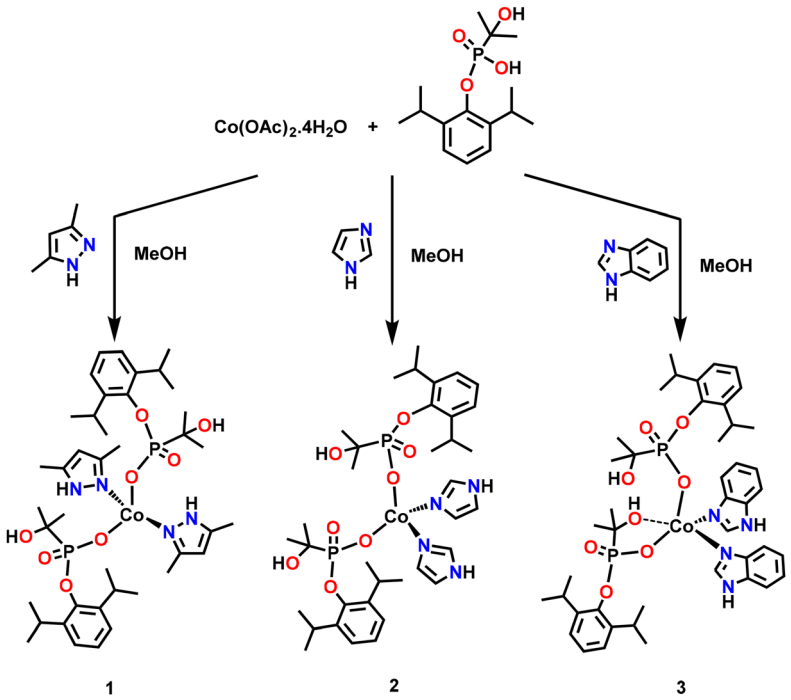

Scheme 1 Synthesis of mononuclear Co(II) phosphonates **1–3**.

phosphonates and the formation of metal–oxygen bonds. The weak absorption bands in the range 3000–2800 cm^{-1} are due to the unsaturated as well as saturated C–H stretching frequencies of the alkyl group of ligands. The band appearing around 1600–1400 cm^{-1} reveals the presence of conjugated C=C functional groups. The characteristic P=O and O–P–O stretching vibrations and M–O–P asymmetric and symmetric vibrations appear at 1161, 1051, and 916 cm^{-1} for complex **1**. Similarly, complexes **2–3** show bands in the range of 1172–1174 cm^{-1}, which are because of O–P–O stretching vibrations. Sharp absorption bands around 1059 and 1050 cm^{-1} are due to M–O–P asymmetric and symmetric vibrations, respectively (Fig. S1). The thermal decomposition studies of **1–3** were carried out through thermogravimetric analysis (TGA) at temperatures ranging from 25 to 800 °C at a heating rate of 10 °C min^{-1} under a nitrogen atmosphere (Fig. S2). The first weight loss was observed for compound **1** at 140 °C, for **2** at 203 °C and for **3** at 205 °C. These weight losses correspond to the alkyl and aryl groups of the phosphonates and N-donor ligands, respectively.

UV-Vis absorption spectra were recorded under ambient conditions for complexes **1–3** in methanol. The spectra exhibited two or three absorption maxima in the 200–290 nm range attributed to π–π^* electronic transitions occurring in the ligand moieties of **1–3** (Fig. S3). The weak absorption band detected in the visible region 450–700 nm is consistent with d–d transitions of tetrahedral cobalt(II) complexes. Powder X-ray diffraction studies (PXRD) for **1–3** indicated good agreement between experimental and simulated patterns, indicating the bulk sample phase purity (Fig. S4). Elemental analysis results of **1–3** matched well with the calculated values, verifying their purity (Fig. S5–S7).

Molecular structure of $[Co(HL)_2(dmpz)_2]$ (1)

Blue-coloured cube-shaped crystals of **1** suitable for X-ray diffraction were directly obtained from the reaction mixture in a week by slow evaporation of methanol at room temperature. Single-crystal X-ray diffraction studies reveal that **1** crystallizes in the monoclinic $P2_1/c$ space group. The asymmetric part of the unit cell is occupied by two chemically similar but crystallographically different molecules, each consisting of one cobalt ion, two 3,5-dmpz molecules and two singly deprotonated phosphonate molecules (HL). Each cobalt ion is surrounded by two nitrogens from 3,5-dmpz and two oxygens from the phosphonate ligands. SHAPE analysis was carried out to confirm the coordination geometry around the cobalt(II) ion (Table S1). The cobalt centre in **1** shows a 0.049 deviation from an ideal tetrahedron. The Co–O bond length (1.943(3) Å) and the Co–N distances (2.000(3) Å and 2.007(3) Å) in **1** (Fig. 1) are comparable to distances observed in similar cobalt(II) tetrahedral complexes.[51,52] The nearest Co(II) ions within the lattice are separated by more than 9.741(2) Å (Fig. S8). Selected bond angles and bond lengths for **1** are listed in Table S3. The intermolecular hydrogen bonding *via* O8···N4–H4 further extends, forming a 1-D network. Inter- and intra-molecular hydrogen-bonding distances in **1** are listed in Table S4.

Molecular structure of $[Co(HL)_2(imz)_2]$ (2)

Blue-coloured needle-like crystals of **2** suitable for X-ray diffraction were directly obtained from the reaction mixture by slow

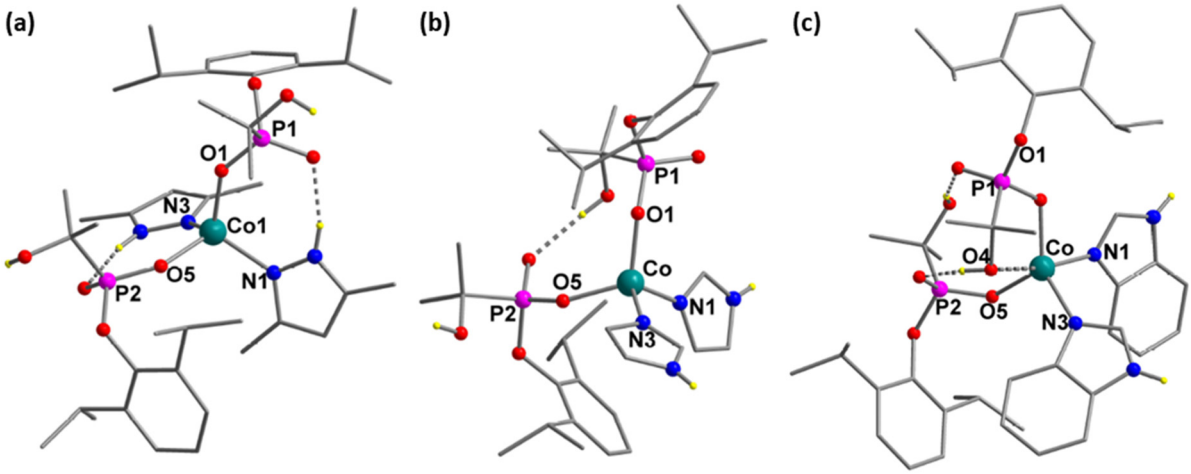

Fig. 1 (a) Molecular structures of (a) **1**, (b) **2**, and (c) **3** (H atoms attached to the carbon atoms have been omitted for clarity).

evaporation of methanol at room temperature in 7–8 days. Single crystal X-ray diffraction studies conducted at 100 K reveal that **2** crystallizes in the monoclinic $P2_1/n$ space group. The asymmetric part of the unit cell is occupied by one cobalt ion, two imidazole moieties, and two HL molecules, as shown in Fig. 1. Each cobalt ion is surrounded by two nitrogens from imidazole and two oxygens from the phosphonate-based HL ligands. The arrangement around Co(II) is tetrahedral as confirmed by SHAPE analysis (Table S1). The Co–O bond length (1.918(1) Å–1.935(1) Å) and the Co–N distance (1.997(2) Å–2.010(2) Å) in **2** are comparable to distances observed in similar Co(II) tetrahedral complexes. Similarly, the P1–O1 (1.496(1) Å) and P1–O3 (1.609(1) Å) distances around the phosphorus indicate delocalisation of the negative charge over the O1–P1–O3 segment. The nearest cobalt(II) ions within the lattice are separated by more than 6.1766(7) Å (Fig. S10). Intermolecular hydrogen bonding occurs between N–H and O3 and between the hydrogen of O–H of phosphonates and O7, further extending to form a 2-D network (Fig. S9). Intramolecular hydrogen-bonding distances are listed in Table S4.

Molecular structure of $[Co(HL)_2(bimz)_2]$ (3)

Violet-coloured block-shaped crystals of **3** were obtained after recrystallization in acetonitrile in two weeks by slow evaporation at room temperature. Complex **3** crystallizes in the monoclinic space group $P2_1/n$ with one molecule occupying the asymmetric part of the unit cell that comprises one cobalt ion, two HL ligands and two benzimidazole molecules as shown in Fig. 1. Each cobalt ion is surrounded by two nitrogens from benzimidazole (Co–N bond lengths 2.054(3)–2.086(3) Å), two oxygens from the phosphonate-based HL ligands (Co–O bond lengths 1.997(3)–2.011(3) Å) and the O4 atom of the hydroxy group of one phosphonate with an unusually long bond of 2.327(3) Å (Co–O4). The negative charge of the counterion (HL) is delocalised between the two oxygen atoms O1-O2 and O5-O6. Intramolecular hydrogen-bonding distances for **3** are listed in Table S4. The separation between the two nearest Co (II) ions is 7.757(2) Å (Fig. S11). The molecule in the asymmetric unit occupies a distorted tetrahedral geometry around the Co(II) ion and is confirmed by SHAPE analysis (Fig. 2).

Static magnetic properties and X-band EPR measurements

Magnetic susceptibility measurements for complexes **1–3** were conducted on polycrystalline powdered samples between 1.8 and 300 K at an applied dc field of 0.1 T. At room temperature, $\chi_M T$ values are 2.45, 2.45 and 2.65 cm^3 K mol^{-1} for **1–3**, respectively. The obtained $\chi_M T$ values are higher than the expected spin-only value (S = 3/2, g = 2.0; 1.875 cm^3 K mol^{-1}) of one isolated Co(II) high-spin centre, indicating the presence of spin–orbit coupling. Upon cooling, the $\chi_M T$ value remains almost constant until 30 K, and subsequently a rapid decline of the $\chi_M T$ value to 1.39 cm^3 K mol^{-1} at 1.8 K for complex **1** can be associated with the presence of intrinsic magnetic anisotropy and ZFS of the cobalt(II) ions. Given that the nearest separation found between the Co···Co in the lattice is 9.741(2) Å for **1**, the intermolecular exchange can be neglected. Magnetization data were obtained at different temperatures and dc fields up to 7 T. The reduced magnetization plots at various temperatures do not overlap, and the high-field magnetisation does not saturate, which suggests that the complexes under study exhibit magnetic anisotropy. The magnetization values reach 2.04μ_B (**1**), 2.56μ_B (**2**), and 2.24μ_B (**3**) at 7 T, which are lower than the theoretical value of 3.0μ_B (S = 3/2, g = 2.0). The spin Hamiltonian (eqn (1)) was applied for fitting the magnetic susceptibility data and the variable-field variable-temperature magnetisation data (Fig. 3) with the help of julX_2s (Fig. S12–S16).

The X-band EPR spectra were recorded on polycrystalline samples. The EPR spectrum of **1** shows broad EPR transitions with approximate effective g values of 6.71, 1.18, and 0.87, exhibiting partially resolved hyperfine splitting in low field. The EPR spectrum of complex **2** at 5 K exhibits a characteristic pattern of distorted tetrahedral cobalt(II) complexes with g

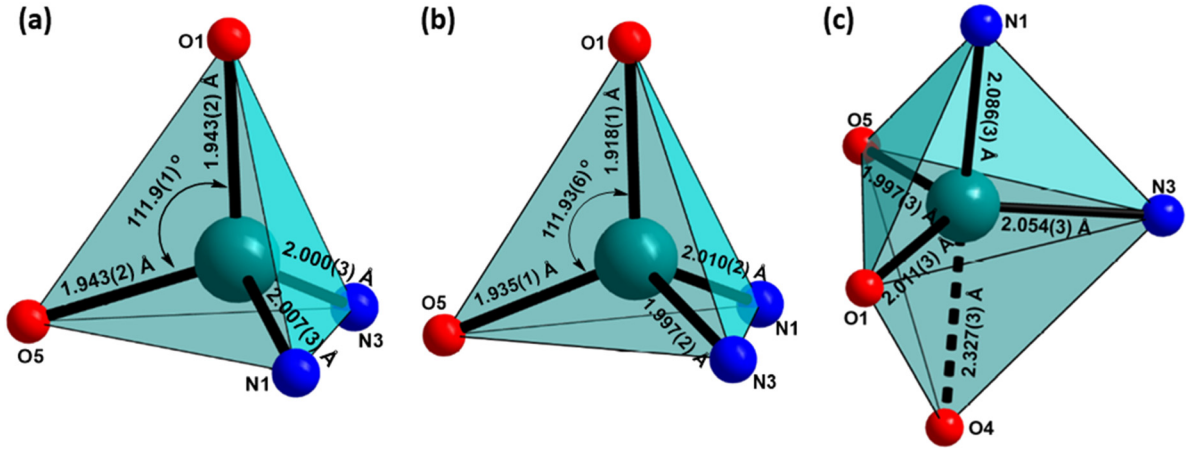

Fig. 2 Polyhedral view of the coordination environment around Co(II) centres: (a) **1**, (b) **2** and (c) **3**.

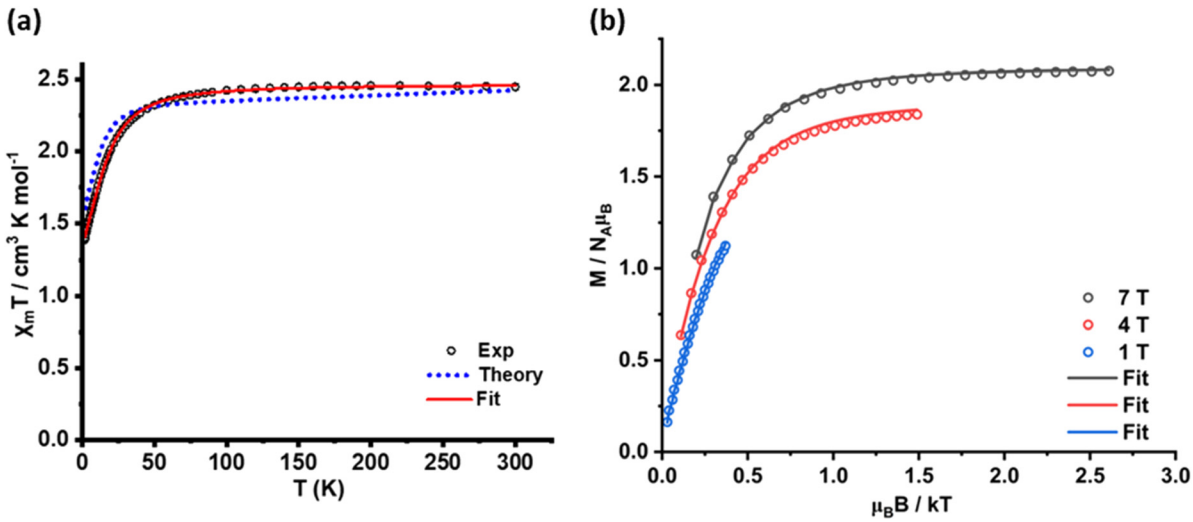

Fig. 3 (a) Temperature-dependent χ_MT plot for **1** measured under an applied dc field of 0.1 T. The solid line is the best fit, and the dotted line represents simulated χ_MT values with CASSCF/NEVPT2 calculations. (b) Variable-temperature variable-field magnetization for complex **1**. The solid lines are the best fits.

values of 6.21, 1.95, and 1.55 (Fig. S17).[53] The spectrum shows hyperfine splitting, which can be correlated with a negative sign of D extracted from the variable-temperature magnetic susceptibility plot. For complex **3**, EPR spectral features are different from those of **1** and **2** and show a large rhombicity parameter (E/D = 0.25) associated with the mixing of Kramers doublets (KDs).[54] The g values for **3** are 6.45, 2.52, and 0.87. It is difficult to accurately determine the magnitude of ZFS using conventional EPR experiments. However, the sign of magnetic anisotropy can be explained.[55]

Dynamic magnetic properties

Alternating-current (ac) susceptibility measurements were carried out to understand the magnetic relaxation dynamics of complexes **1–3** with an oscillating field of 3.5 Oe. No frequency-dependent out-of-phase ac susceptibility signals (χ'') were observed under a zero static magnetic field. This indicates a fast relaxation process, resulting from quantum tunnelling of magnetization (QTM), which can be suppressed by applying external magnetic fields. To determine the optimum magnetic field, the field-dependent and frequency-dependent ac susceptibility was measured at 1.8 K in the frequency range of 0.1–1000 Hz at various magnetic fields. Upon application of optimized external fields, the out-of-phase (χ'') frequency-dependent ac susceptibility maxima were observed, indicating field-induced SIM behaviour. χ' *vs.* χ'' was plotted to generate Cole–Cole plots and then fitted using the generalized Debye function to extract α and τ values. The α parameter (Table S5) shows a narrow distribution of relaxation times ($0.13 < \alpha < 0.28$) for complex **1**. The linear region of the high-temperature part of the $\ln(\tau)$ *vs.* $1/T$ data was fitted using the Arrhenius equation, $\tau = \tau_0 \exp(U_{eff}/k_BT)$, assuming the Boltzmann con-

stant (k_B) to be unity, yielding an effective energy barrier U_{eff} = 31.9 K and a pre-exponential factor $\tau_0 = 1.41 \times 10^{-7}$ s. The plot of all temperatures was fitted using the equation:

$$\tau^{-1} = \tau_{QTM}^{-1} + AH^4T + CT^n + \tau_0^{-1} \exp(-U_{eff}/k_BT)$$

For complex **1**, the magnetic dynamics is dominated by three relaxation processes: Orbach, Raman and QTM (Fig. 4). The best fit yields values of the Raman parameters $C = 0.29$ s^{-1} K^{-n}, $n = 8.7$ and $\tau_{QTM} = 39.04$ s. In contrast, for complexes **2** and **3**, the Orbach and Raman relaxation processes are predominant (Fig. S20 and S22). The best fit for **2** yields a U_{eff} of 32.5 K and a pre-exponential factor (τ_0) of 3.9×10^{-11} s, $n = 5.5$, and $C = 13.28$ s^{-1} K^{-n}, and for **3**, $U_{eff} = 26.2$ K, $\tau_0 = 1.67 \times 10^{-6}$ s, $n = 2.5$, and $C = 12.15 \times 10^2$ s^{-1} K^{-n} (Fig. S20 and S22). Complex **2** shows high rhombicity and small τ_0, indicating enhanced transverse anisotropy that promotes faster relaxation, requiring a higher static field to suppress these pathways.

Estimation of the ZFS parameter using *ab initio* calculations

To understand the magnetic properties of complexes **1**, **2**, and **3**, we carried out *ab initio* calculations using the CASSCF/NEVPT2 methods implemented in ORCA 6.0 (see Computational details for more information). These calculations provided the values of the axial ZFS parameter (D), the rhombicity ratio (E/D), and the g-tensor components (summarised in Table 2). Importantly, the computed parameters agreed well with experimental magnetic susceptibility data (refer to Fig. 3, Figs. S12–S16, Table 1, and Fig. 5).

In an ideal T_d symmetry, the ligand field terms are $^4A_2$(F), $^4T_2$(F), $^4T_1$(F), and $^4T_1$(P). However, due to the pseudo-C_2 symmetry of complexes **1–3**, these terms transform into ^{4}A, {^{4}A and two ^{4}B} (F), and {^{4}A and two ^{4}B} (P), respectively. The three states {^{4}A and two ^{4}B} (F), derived from the $^4T_2$(F) term, correspond to the first excited states, while the ^{4}A state originating from the $^4A_2$(F) term serves as the ground state.

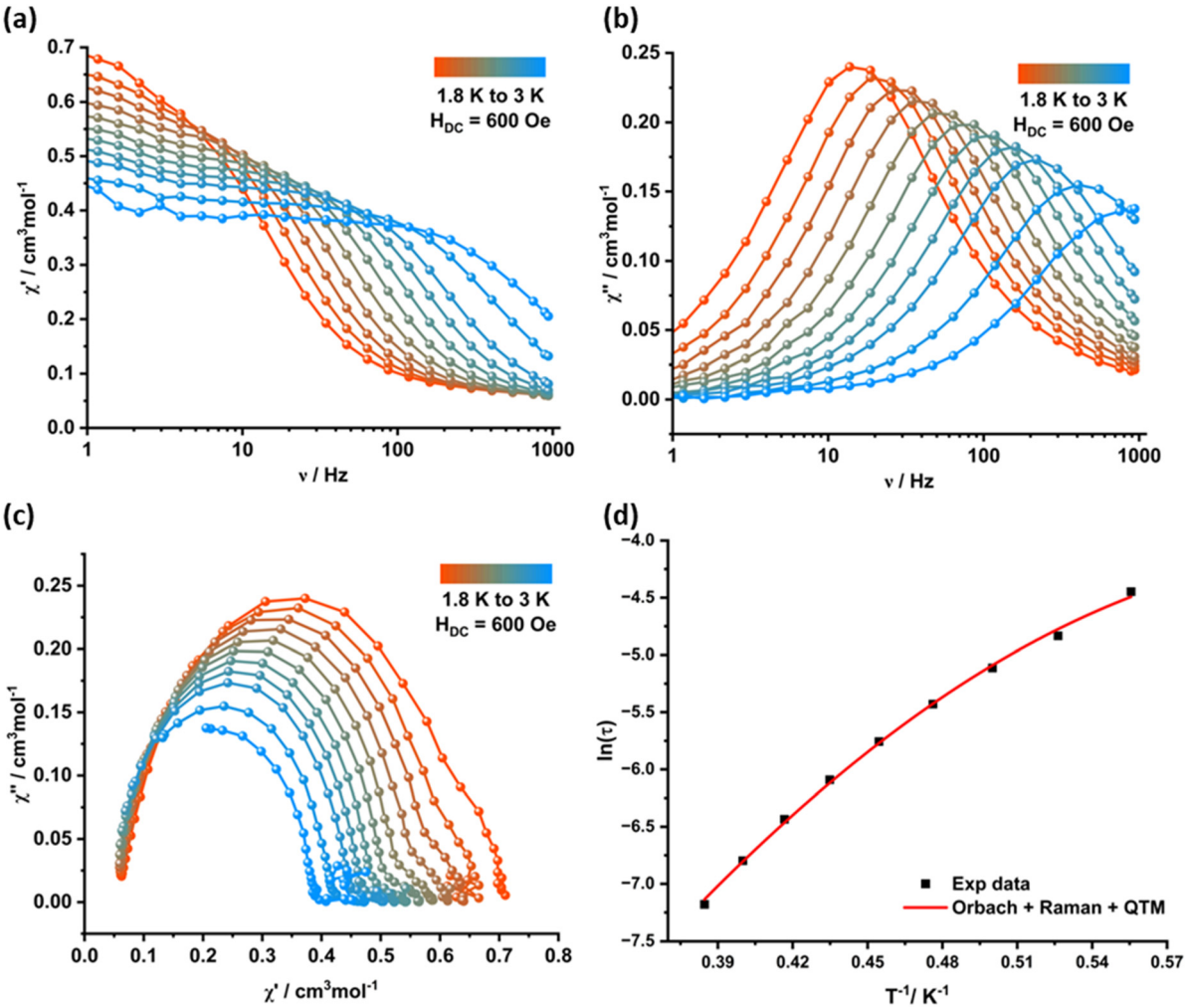

Fig. 4 (a) In-phase (χ'_M) and (b) out-of-phase (χ''_M) components of the frequency-dependent (0.1–1000 Hz) ac susceptibility measured over the temperature range of 1.8–3 K in an oscillating ac field of 3.5 Oe and an applied dc field of 600 Oe for **1**. (c) Cole–Cole plots for **1** under an applied dc field of 600 Oe. The solid lines are guides to the eye. (d) The plot of the relaxation time τ (logarithmic scale) *versus* T^{-1} for **1**; the solid red line corresponds to the best fit to the Orbach, Raman, and QTM processes.

Table 1 Summary of the various magnetic parameters determined experimentally and obtained using CASSCF/NEVPT2

	Experimental values					CASSCF/NEVPT2	
Comp.	D (cm^{-1})	E/D	U_{eff} (K)	τ_0 (s)	H_{dc} (Oe)	D (cm^{-1})	E/D
1	−18.9	0.02	31.9	1.41×10^{-7}	600	−15.1	0.03
2	−13.7	0.11	32.5	3.99×10^{-11}	1000	−12.3	0.18
3	+22.3	0.25	26.2	1.67×10^{-6}	300	+22.6	0.27

Table 2 CASSCF- and NEVPT2-computed SH parameters (D and $|E/D|$)

Complex	D (CASSCF) (cm^{-1})	E/D (CASSCF)	D (NEVPT2) (cm^{-1})	E/D (NEVPT2)
1	−16.6	0.04	−15.1	0.03
2	−14.2	0.19	−12.3	0.18
3	23.3	0.26	22.6	0.27

To understand how these values arise, the state-wise contributions to D were examined (Table 3), highlighting that the $^4T_2(F)$ state is the primary contributor. As shown in Table 3, for complexes **1** and **2**, the two major contributions from the $^4T_2(F)$ state are negative, whereas for complex **3**, they are positive, indicating a gradual reduction in the negative contribution to D from **1** to **3**. It is well known that transitions between orbitals with different m_l values contribute to a positive D value, while spin-conserved transitions between orbitals with the same m_l value result in a negative D value.[48,56–59] To further elucidate the electronic origin of this anisotropy, *Ab Initio* Ligand Field Theory (AILFT) analysis was performed. AILFT projects the multiconfigurational wavefunction onto a ligand field basis, yielding energy levels of the d-orbitals in the principal axis frame of the D-tensor. These orbital energy splittings and occupations, derived from natural orbital analysis, are shown in Fig. 6 for the ground state of each complex. The observed increase in ligand field splitting in complex **3** is attributed to an additional donor atom.

In addition to these energetic considerations, the ground-state wavefunctions show significant multideterminant character, meaning that the electronic configuration is not a single, pure arrangement of electrons, but a weighted mixture of several configurations. The dominant electronic configuration for the ground state of complex **1** is $\{(d_{x^2-y^2})^2(d_{z^2})^1(d_{yz})^2(d_{xz})^1(d_{xy})^1\}$ (55%), whereas the first excited state is $\{(d_{x^2-y^2})^2(d_{z^2})^1(d_{yz})^1(d_{xz})^2(d_{xy})^1\}$ (62%). Similarly, for **2**, the ground state and first excited state are $\{(d_{x^2-y^2})^1(d_{z^2})^1(d_{yz})^2(d_{xz})^1(d_{xy})^2\}$ (50%) and $\{(d_{x^2-y^2})^1(d_{z^2})^1(d_{yz})^1(d_{xz})^2(d_{xy})^2\}$ (55%), respectively. In contrast, complex **3** exhibits a ground state of $\{(d_{x^2-y^2})^2(d_{z^2})^2(d_{xz})^1(d_{yz})^1(d_{xy})^1\}$ (58%) and a first excited state of $\{(d_{x^2-y^2})^2(d_{z^2})^1(d_{xz})^2(d_{yz})^1(d_{xy})^1\}$ (56%). Additional AILFT-based details for both the ground and first excited states of complexes **1–3** are provided in Fig. S24 of the SI.

Magneto-structural D correlation

To gain a deeper understanding of the factors influencing the sign of the axial zero-field splitting parameter (D) beyond the well-known electronic transitions involving different magnetic quantum numbers (m_l), we carried out a detailed magneto-structural correlation analysis on cobalt(II) complexes **1–3**. Although all three complexes exhibit a similar chemical environment around the Co(II) center, an intriguing variation in the sign of D is observed: complexes **1** and **2** exhibit negative D values, whereas complex **3** shows a positive D value.

To begin with, we have performed DFT-based AIM analysis that indicates that complex **3** features an additional interaction between Co1 and O4, absent in complexes **1** and **2** (see the SI). Although not a true covalent bond, the $|V(r)/G(r)|$ ratio suggests an ionic character, as can be presented best as a pseudo-bond compared to others. This raised the question: could this extra bond be responsible for the change in the sign of D? To explore this, we performed computational experiments where the Co1–O4 bond length in complex **3** was gradually increased from 2.33 Å to 3.34 Å. Interestingly, despite this alteration, the sign of D remained positive. Similarly, we reduced comparable bond distances in complexes **1** and **2** to

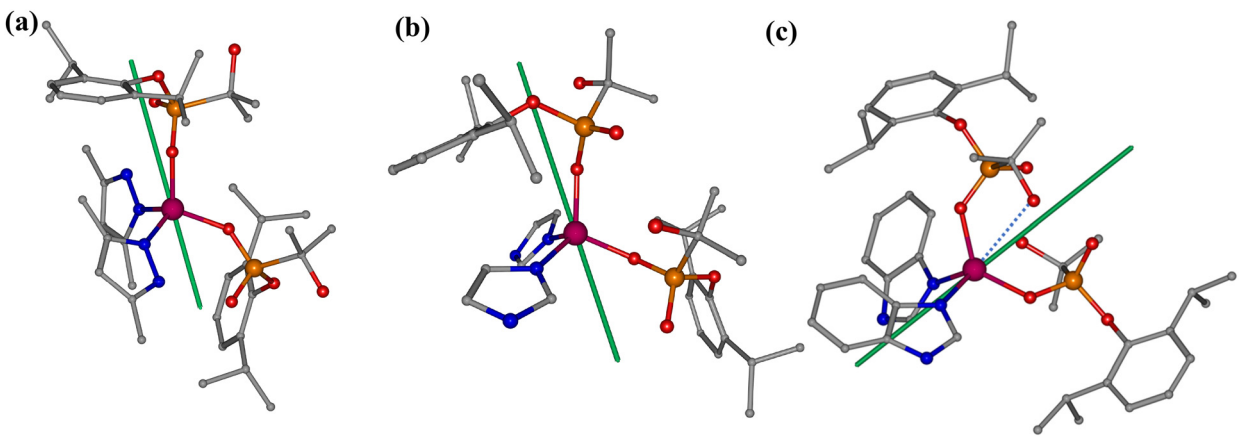

Fig. 5 NEVPT2-calculated orientation of the main magnetic axes (D_{zz}) for (a) **1**, (b) **2**, and (c) **3**. Colour code: Co (deep magenta); O (red); N (blue); C (gray); and P (orange). Here, hydrogens are omitted for clarity.

Table 3 State-by-state contributions to the D values (cm^{-1}) and the SH parameters (g, D, and $|E/D|$) were estimated *via* CASSCF (7, 5) + NEVPT2

	1		2		3	
State	CASSCF	NEVPT2	CASSCF	NEVPT2	CASSCF	NEVPT2
$^4T_2(F)$	−38.7	−34.1	−32.3	−26.4	11.7	11.6
	10.0	8.3	13.0	10.6	3.3	3.3
	11.8	9.5	6.3	4.6	8.1	7.7
^2G	5.2	5.4	2.7	2.5	−1.9	−1.9
	−2.2	−2.2	−1.9	−1.9	−2.3	−2.3
	−2.6	−2.6	−1.9	−1.7	4.2	4.2
D_{tot}	−16.6	−15.1	−14.2	−12.3	23.3	22.6
E/D	0.04	0.03	0.19	0.18	0.26	0.27
g_{xx}	2.24	2.20	2.21	2.17	2.13	2.10
g_{yy}	2.25	2.21	2.28	2.24	2.32	2.27
g_{zz}	2.43	2.39	2.39	2.33	2.56	2.46

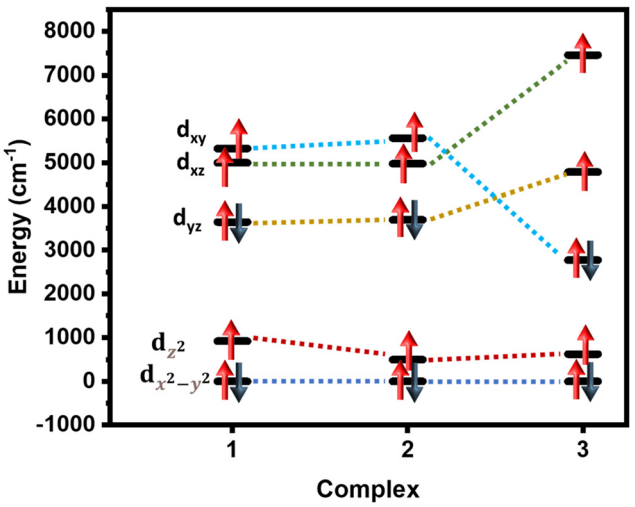

Fig. 6 Ground-state comparative energies of the d orbitals in complexes **1–3** derived from AILFT analysis.

check for any sign reversal in D, but again, no change was observed (see Table S9 and Fig. S23 in the SI). These results strongly suggest that the presence of the additional Co–O bond in complex **3** is not the primary reason for its positive D value.

Next, we turned our attention to more subtle geometric factors. By closely examining the first coordination sphere (*i.e.*, the immediate bonding environment around the cobalt center), we observed noticeable differences in both bond lengths and bond angles across the three complexes. One standout feature was the Co–O–P bond angle, which differed significantly: approximately 141° and 140° in complexes **1** and **2**, respectively, but only 118° in complex **3**. Given the limited dataset (only three complexes), we systematically modified the first coordination sphere geometry and the Co–O–P bond angle to generate a broader dataset for correlation (see Table S10 in the SI). These controlled modifications allowed us to evaluate how such structural variations influence D. Literature reports have proposed several magneto-structural correlations for tetrahedral Co(II)-based single-ion magnets (SIMs), often focusing on deviations from the ideal tetrahedral angle of 109.5°, such as axial elongation and bite or cis angles.[45,56,60–63] We attempted to apply similar correlations by calculating the average deviation of the six coordination angles from the ideal 109.5° in our systems. However, some complexes did not follow this trend, and the sign of D could not be reliably predicted using this approach alone (see Fig. S9 in the SI).

To improve this, we introduced a new structural parameter, δ, which incorporates both the average angular deviation from ideal tetrahedral geometry and the Co–O–P bond angle. The parameter δ is defined as

$$\delta = \frac{1}{6}\sum |109.5° - \theta| + 150 - \theta'$$

where θ = bond angles around the metal center (typically 6 for a tetrahedral geometry), θ' = Co–O–P bond angle, and 109.5° is the ideal tetrahedral bond angle. Using the δ value, we can determine the sign of D; particularly when δ is less than 20, the sign will be negative and if δ is more than 20, the sign will be positive. This correlation holds true not only for the original three complexes but also for all systematically modified geometries, as illustrated in Fig. 7. Thus, by introducing the Co–O–P bond angle into the magneto-structural analysis, we established a more robust and predictive framework for understanding and tuning the sign of D in tetrahedral Co(II) SIMs.

Conclusions

To conclude, we have synthesized three distinct mononuclear cobalt(II) complexes **1–3** incorporating different N-donor ligands, which have been characterized by various analytical and spectroscopic techniques. Their molecular structures have also been established by single-crystal X-ray diffraction studies. The study of high-temperature magnetic susceptibility data of complexes **1–3** indicated behaviour characteristic of paramagnetic high-spin Co(II) ions. At low temperature, magnetic susceptibility behaviour was influenced by the ZFS effect. *Ab initio* CASSCF/NEVPT2 calculations have been employed to probe the relationship between the magnetic anisotropy and the electronic and geometric structures. A comparative magneto-struc-

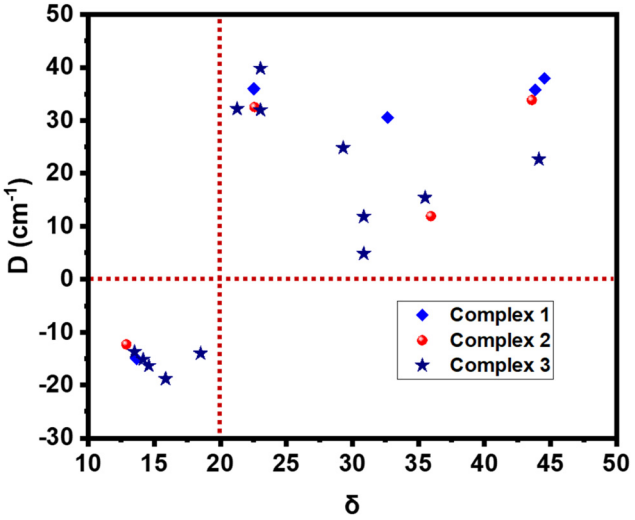

Fig. 7 Correlation between δ and computed D values for Co(II) complexes **1–3** and their variants. A δ threshold of 20 (dashed line) clearly separates positive and negative D values.

tural analysis (using dc magnetic and theoretical calculations) indicates that in complex **3** the positive D value may result from the combined effect of distortion from the ideal tetrahedral angle and a smaller Co–O–P bond angle. All complexes were investigated for single-ion magnet (SIM) behaviour, with complexes **1–3** exhibiting field-induced slow magnetic relaxation.

Experimental section

General characterization

All chemicals and solvents were used as purchased from commercial sources. Cobalt acetate tetrahydrate [$Co(OAc)_2{\cdot}4H_2O$] (Loba Cheme), imidazole (Merck) and benzimidazole (Spectrochem) were used as procured. The ligand [(2,6-$^{i}Pr_2C_6H_3O$)P(O)(OH)(CMe_2(OH))] (**H_2L**) and 3,5-dimethylpyrazole (dmpz) were synthesized employing previously reported procedures.[64,65] Melting points were measured in glass capillaries on a hot-stage microscope and are reported uncorrected. CHN elemental analysis was performed on an Elementar Analysensysteme GmbH (Vario MICRO cube) microanalyzer. Fourier transform infrared (FT-IR) spectra were recorded with a PerkinElmer Spectrum One FT-IR spectrometer using KBr-diluted discs. UV-Visible spectra were recorded using an Agilent Cary UV-VIS-NIR (RM360) spectrophotometer. The phase purity of bulk material was checked by powder X-ray diffraction (PXRD) measurement, performed on a Rigaku SmartLab SE diffractometer using Cu Kα (λ = 1.54190 Å) radiation. For thermogravimetric analyses (TGA), the samples were heated up to 800 °C at a heating rate of 10 °C min^{-1} under a nitrogen atmosphere and simultaneously measured using a Rigaku STA8122 Thermo plus EVO2 thermal analysis system. X-band electron paramagnetic resonance (EPR) studies were conducted using a Bruker EMX plus EPR spectrometer at 5 K.

Single-crystal X-ray diffraction studies

The single crystal X-ray diffraction of **1–3** was recorded using a Bruker D8 QUEST single-crystal diffractometer equipped with an IμS DIAMOND microfocus Mo Kα (λ = 0.7107 Å) radiation source. The CrysAlisPro[66] software suite was used for data collection, data integration and indexing. The structures of the complexes were solved by using direct methods (ShelXT)[67] using the OLEX2[68] module, and the crystal structure was refined using full-matrix least-squares techniques with the ShelXL[69] program. All non-hydrogen atoms were refined anisotropically. The data collection and structure refinement details are summarized in Table S1. The coordination geometry analysis was carried out using SHAPE2.1[70] software. Diamond 3.2[71] software was used for structure representation.

Magnetic measurements

All the magnetic susceptibility measurements were carried out on the polycrystalline ground samples packed in a polycarbonate capsule inside a non-magnetic sample holder, using a Quantum-Design MPMS3 SQUID magnetometer. Diamagnetic corrections were applied for the sample holder. Direct-current (dc) susceptibility measurements were performed over the temperature range of 1.8–300 K. Data obtained from dc measurements were fitted using the JulX-2S program.[72] Dynamic susceptibility measurements were carried out at frequencies between 0.1 and 1000 Hz with a 3.5 Oe oscillating field.

Computational details

The X-ray structures served as the foundation for all quantum chemistry calculations performed using ORCA6.0.[73] Multireference *ab initio* computations were employed to investigate the nature of low-lying excited states and determine the zero-field splitting (ZFS) parameters. For complexes **1–3**, CASSCF calculations combined with N-electron valence perturbation theory (NEVPT2) were conducted. Dynamic correlation effects were incorporated by performing NEVPT2 calculations on top of the converged CASSCF wavefunctions. Scalar relativistic effects were addressed using the second-order Douglas–Kroll–Hess (DKH) method. All calculations utilized the def2-TZVP basis set for Co, O, and N, while the def2-SVP basis set was applied to the remaining atoms.[74–76] Computational efficiency was enhanced through the use of auxiliary basis sets and the resolution of identity (RI) approximation. Given that the D values for **1–3** exhibited consistent trends in both model structures and magneto-structural correlations, only CASSCF calculations were performed. The active space CAS(7,5) was employed to compute ten quartet and forty doublet states. In addition to evaluating spin-Hamiltonian (SH) parameters, magnetization data were analysed to assess the accuracy of the computational fit. We have employed AIM analysis to determine the metal–ligand bonding and identify the bond critical

points (BCPs), a method widely recognised for evaluating the nature of bonding in transition metal complexes.[77,78]

Synthesis of 1

$Co(OAc)_2{\cdot}4H_2O$ (62.25 mg, 0.25 mmol) was dissolved in 10 mL of methanol, to which 10 mL of a methanolic solution of $\mathbf{H_2L}$ (150 mg, 0.5 mmol) was added under stirring. After 15 minutes of vigorous stirring, 48 mg (0.5 mmol) of 3,5-dimethylpyrazole was added and stirring was continued for an additional 2 h; subsequently, the solution was left undisturbed for crystallization. Over a period of 4–5 days, blue crystals of **1** were formed through slow evaporation of the solvent. Mp. ~160 °C. Yield: 130 mg (61%, based on metal). Anal. calc. for $C_{40}H_{64}CoN_4O_8P_2$ (Mr = 849.85): C, 56.53; H, 7.59; N, 6.59%. Found: C, 56.24; H, 7.54; N, 6.30%. FT-IR (KBr, cm^{-1}): ν: 3395 (br), 2967(s), 2927(s), 2867(m), 1592(m), 1465(s), 1441(s), 1384(m), 1255(m), 1161(vs), 1051(vs), 916(s), 763(m), 673(m), 568(w). UV–Vis (MeOH) λ, nm (ε M^{-1} cm^{-1}): 266 (1.76×10^2), 518 (17).

Synthesis of 2

Complex **2** was prepared following the procedure for complex **1**, using imidazole (68 mg, 1 mmol) in place of 3,5-dimethylpyrazole. Blue-coloured crystals were obtained in a week. Mp. ~220 °C. Yield: 131 mg (66%, based on metal). Anal. calc. for $C_{36}H_{56}CoN_4O_8P_2$ (Mr = 793.74): C, 54.48; H, 7.11; N, 7.06%. Found: C, 53.78; H, 7.26; N, 6.78%. FT-IR (KBr, cm^{-1}): ν: 3348 (br), 3130(m), 3047(m), 2964(s), 2866(m), 1553(m), 1465(m), 1437(w), 1385(s), 1259(m), 1172(vs), 1072(vs), 1059(vs), 916(s), 741(m), 655(m), 517(w). UV–Vis (MeOH) λ, nm (ε M^{-1} cm^{-1}): 265 (8.3×10^2), 530 (17).

Synthesis of 3

Complex **3** was synthesized following the same procedure described above for **1** using benzimidazole (118 mg, 1 mmol). However, slow evaporation of solvent yielded a precipitate, which was subsequently redissolved in acetonitrile to isolate violet colour single crystals suitable for X-ray diffraction in 2 weeks. Mp. ~205 °C. Yield: 93 mg (42%, based on metal). Anal. calc. for $C_{44}H_{60}CoN_4O_8P_2$ (Mr = 893.86): C, 59.12; H, 6.77; N, 6.27%. Found: C, 58.89; H, 6.66; N, 6.27%. FT-IR (KBr, cm^{-1}): ν: 3248(br), 3075(w), 3031(w), 2967(s), 2876(m), 1598(w), 1436(s), 1335(m), 1257(m), 1174(vs), 1050(vs), 916(vs), 748(s), 675(m), 570(m). UV-Vis (MeOH) λ, nm (ε M^{-1} cm^{-1}): 243 (7.73×10^3), 533 (98).

Conflicts of interest

There are no conflicts to declare.

Data availability

The data supporting this article have been included as part of the SI. Supplementary information is available. See DOI: https://doi.org/10.1039/d5dt01461a.

CCDC 2448658–2448660 (**1–3**) contain the supplementary crystallographic data for this paper.[79a–c]

Acknowledgements

R. M. acknowledges financial support from SERB, New Delhi, through CRG/2022/002406 and SB/S2/JCB-85/2014. A. P. thanks UGC, New Delhi, for a research fellowship. R. R. acknowledges the Prime Minister's Research Fellowship (PMRF) for a research fellowship. The authors thank the MoE IoE-funded PPMS, MPMS, and EPR central facilities for characterization data. G. R. thanks SERB for funding (SB/SJF/2019-20/12; CRG/2022/001697).

References

1 F. D. Natterer, K. Yang, W. Paul, P. Willke, T. Choi, T. Greber, A. J. Heinrich and C. P. Lutz, *Nature*, 2017, **543**, 226–228.
2 M. Mannini, F. Pineider, P. Sainctavit, C. Danieli, E. Otero, C. Sciancalepore, A. M. Talarico, M.-A. Arrio, A. Cornia and D. Gatteschi, *Nat. Mater.*, 2009, **8**, 194–197.
3 R. E. Winpenny, *Angew. Chem., Int. Ed.*, 2008, **47**, 7992–7994.
4 R. Sessoli, D. Gatteschi, A. Caneschi and M. Novak, *Nature*, 1993, **365**, 141–143.
5 M. Atzori and R. Sessoli, *J. Am. Chem. Soc.*, 2019, **141**, 11339–11352.
6 A. Gaita-Ariño, F. Luis, S. Hill and E. Coronado, *Nat. Chem.*, 2019, **11**, 301–309.
7 L. Bogani and W. Wernsdorfer, *Nat. Mater.*, 2008, **7**, 179–186.
8 M. Urdampilleta, S. Klyatskaya, J.-P. Cleuziou, M. Ruben and W. Wernsdorfer, *Nat. Mater.*, 2011, **10**, 502–506.
9 C. Cervetti, A. Rettori, M. G. Pini, A. Cornia, A. Repollés, F. Luis, M. Dressel, S. Rauschenbach, K. Kern and M. Burghard, *Nat. Mater.*, 2016, **15**, 164–168.
10 S. Rao, J. Ashtree and A. Soncini, *Phys. Rev. B:Condens. Matter*, 2020, **592**, 412237.
11 M. Murugesu, M. Habrych, W. Wernsdorfer, K. A. Abboud and G. Christou, *J. Am. Chem. Soc.*, 2004, **126**, 4766–4767.
12 A. J. Tasiopoulos, A. Vinslava, W. Wernsdorfer, K. A. Abboud and G. Christou, *Angew. Chem., Int. Ed.*, 2004, **43**, 2117–2121.
13 O. Waldmann, *Inorg. Chem.*, 2007, **46**, 10035–10037.
14 F. Neese and D. A. Pantazis, *Faraday Discuss.*, 2011, **148**, 229–238.
15 G. A. Craig and M. Murrie, *Chem. Soc. Rev.*, 2015, **44**, 2135–2147.

16 M. Feng and M. L. Tong, *Chem. – Eur. J.*, 2018, **24**, 7574–7594.
17 J. Cirera, E. Ruiz, S. Alvarez, F. Neese and J. Kortus, *Chem. – Eur. J.*, 2009, **15**, 4078–4087.
18 P. K. Sahu, R. Kharel, S. Shome, S. Goswami and S. Konar, *Coord. Chem. Rev.*, 2023, **475**, 214871.
19 L. Ungur and L. F. Chibotaru, *Phys. Chem. Chem. Phys.*, 2011, **13**, 20086–20090.
20 D. N. Woodruff, R. E. Winpenny and R. A. Layfield, *Chem. Rev.*, 2013, **113**, 5110–5148.
21 R. J. Blagg, L. Ungur, F. Tuna, J. Speak, P. Comar, D. Collison, W. Wernsdorfer, E. J. McInnes, L. F. Chibotaru and R. E. Winpenny, *Nat. Chem.*, 2013, **5**, 673–678.
22 S. K. Gupta, T. Rajeshkumar, G. Rajaraman and R. Murugavel, *Chem. Sci.*, 2016, **7**, 5181–5191.
23 C. A. Goodwin, F. Ortu, D. Reta, N. F. Chilton and D. P. Mills, *Nature*, 2017, **548**, 439–442.
24 D. E. Freedman, W. H. Harman, T. D. Harris, G. J. Long, C. J. Chang and J. R. Long, *J. Am. Chem. Soc.*, 2010, **132**, 1224–1225.
25 J. M. Zadrozny, D. J. Xiao, M. Atanasov, G. J. Long, F. Grandjean, F. Neese and J. R. Long, *Nat. Chem.*, 2013, **5**, 577–581.
26 A. K. Bar, C. Pichon and J.-P. Sutter, *Coord. Chem. Rev.*, 2016, **308**, 346–380.
27 J. M. Frost, K. L. Harriman and M. Murugesu, *Chem. Sci.*, 2016, **7**, 2470–2491.
28 M. Murrie, *Chem. Soc. Rev.*, 2010, **39**, 1986–1995.
29 J. Goura and V. Chandrasekhar, *Chem. Rev.*, 2015, **115**, 6854–6965.
30 M. G. Walawalkar, H. W. Roesky and R. Murugavel, *Acc. Chem. Res.*, 1999, **32**, 117–126.
31 A. Kumar, A. Ghatak and R. Murugavel, *Dalton Trans.*, 2024, **53**, 14399–14410.
32 R. Murugavel and S. Shanmugan, *Chem. Commun.*, 2007, 1257–1259.
33 R. Murugavel and S. Shanmugan, *Dalton Trans.*, 2008, 5358–5367.
34 R. Murugavel, N. Gogoi and R. Clerac, *Inorg. Chem.*, 2009, **48**, 646–651.
35 K. Sharma, R. Antony, A. C. Kalita, S. K. Gupta, P. Davis and R. Murugavel, *Inorg. Chem.*, 2017, **56**, 12848–12858.
36 S. Hossain, S. K. Gupta and R. Murugavel, *CrystEngComm*, 2015, **17**, 4355–4366.
37 Z.-B. Hu, Z.-Y. Jing, M.-M. Li, L. Yin, Y.-D. Gao, F. Yu, T.-P. Hu, Z. Wang and Y. Song, *Inorg. Chem.*, 2018, **57**, 10761–10767.
38 V. V. Novikov, A. A. Pavlov, Y. V. Nelyubina, M.-E. Boulon, O. A. Varzatskii, Y. Z. Voloshin and R. E. Winpenny, *J. Am. Chem. Soc.*, 2015, **137**, 9792–9795.
39 B. Yao, M. K. Singh, Y.-F. Deng, Y.-N. Wang, K. R. Dunbar and Y.-Z. Zhang, *Inorg. Chem.*, 2020, **59**, 8505–8513.
40 A. Landart-Gereka, M. M. Quesada-Moreno, M. A. Palacios, I. F. Díaz-Ortega, H. Nojiri, M. Ozerov, J. Krzystek and E. Colacio, *Chem. Commun.*, 2023, **59**, 952–955.
41 P. C. Bunting, M. Atanasov, E. Damgaard-Møller, M. Perfetti, I. Crassee, M. Orlita, J. Overgaard, J. van Slageren, F. Neese and J. R. Long, *Science*, 2018, **362**, eaat7319.
42 Y.-S. Meng, Z. Mo, B.-W. Wang, Y.-Q. Zhang, L. Deng and S. Gao, *Chem. Sci.*, 2015, **6**, 7156–7162.
43 X.-N. Yao, J.-Z. Du, Y.-Q. Zhang, X.-B. Leng, M.-W. Yang, S.-D. Jiang, Z.-X. Wang, Z.-W. Ouyang, L. Deng and B.-W. Wang, *J. Am. Chem. Soc.*, 2017, **139**, 373–380.
44 J. M. Zadrozny, J. Telser and J. R. Long, *Polyhedron*, 2013, **64**, 209–217.
45 S. K. Gupta, S. V. Rao, S. Demeshko, S. Dechert, E. Bill, M. Atanasov, F. Neese and F. Meyer, *Chem. Sci.*, 2023, **14**, 6355–6374.
46 M. Idešicová, J. n. Titiš, J. Krzystek and R. Boča, *Inorg. Chem.*, 2013, **52**, 9409–9417.
47 Y. Rechkemmer, F. D. Breitgoff, M. Van Der Meer, M. Atanasov, M. Hakl, M. Orlita, P. Neugebauer, F. Neese, B. Sarkar and J. Van Slageren, *Nat. Commun.*, 2016, **7**, 10467.
48 A. Sarkar, S. Dey and G. Rajaraman, *Chem. – Eur. J.*, 2020, **26**, 14036–14058.
49 S. Vaidya, A. Upadhyay, S. K. Singh, T. Gupta, S. Tewary, S. K. Langley, J. P. Walsh, K. S. Murray, G. Rajaraman and M. Shanmugam, *Chem. Commun.*, 2015, **51**, 3739–3742.
50 G. Bhatt, T. Sharma, S. K. Gupta, F. Meyer, G. Rajaraman and R. Murugavel, *Inorg. Chem.*, 2023, **62**, 18915–18925.
51 G. Peng, Y.-F. Qian, Z.-W. Wang, Y. Chen, T. Yadav, K. Fink and X.-M. Ren, *Cryst. Growth Des.*, 2021, **21**, 1035–1044.
52 S. K. Gupta, S. Kuppuswamy, J. P. Walsh, E. J. McInnes and R. Murugavel, *Dalton Trans.*, 2015, **44**, 5587–5601.
53 L. Banci, A. Bencini, C. Benelli, R. Bohra, J.-M. Dance, D. Gatteschi, V. Jain, R. Mehrotra, A. Tressaud and R. Woolley, *Structures versus Special Properties*, 1982, pp. 37–86.
54 M. H. Pohle, M. Böhme, T. Lohmiller, S. Ziegenbalg, L. Blechschmidt, H. Görls, A. Schnegg and W. Plass, *Chem. – Eur. J.*, 2023, **29**, e202202966.
55 M. H. Pohle, T. Lohmiller, M. Böhme, M. Rams, S. Ziegenbalg, H. Görls, A. Schnegg and W. Plass, *Chem. – Eur. J.*, 2024, **30**, e202401545.
56 S. Vaidya, P. Shukla, S. Tripathi, E. Rivière, T. Mallah, G. Rajaraman and M. Shanmugam, *Inorg. Chem.*, 2018, **57**, 3371–3386.
57 R. Ruamps, L. J. Batchelor, R. Maurice, N. Gogoi, P. Jiménez-Lozano, N. Guihéry, C. de Graaf, A. L. Barra, J. P. Sutter and T. Mallah, *Chem. – Eur. J.*, 2013, **19**, 950–956.
58 S. Gomez-Coca, E. Cremades, N. Aliaga-Alcalde and E. Ruiz, *J. Am. Chem. Soc.*, 2013, **135**, 7010–7018.
59 R. Ruamps, L. J. Batchelor, R. Guillot, G. Zakhia, A.-L. Barra, W. Wernsdorfer, N. Guihéry and T. Mallah, *Chem. Sci.*, 2014, **5**, 3418–3424.
60 C. M. Legendre, E. Damgaard-Møller, J. Overgaard and D. Stalke, *Eur. J. Inorg. Chem.*, 2021, **2021**, 3108–3114.
61 T. Wu, Y.-Q. Zhai, Y.-F. Deng, W.-P. Chen, T. Zhang and Y.-Z. Zheng, *Dalton Trans.*, 2019, **48**, 15419–15426.

62 I. Nemec, R. Herchel, M. Kern, P. Neugebauer, J. Van Slageren and Z. Trávníček, *Materials*, 2017, **10**, 249.
63 M. Böhme, S. Ziegenbalg, A. Aliabadi, A. Schnegg, H. Görls and W. Plass, *Dalton Trans.*, 2018, **47**, 10861–10873.
64 R. Murugavel and S. Kuppuswamy, *J. Chem. Sci.*, 2008, **120**, 131–136.
65 G. Greber, *J. Polym. Sci.*, 1991, **29**, 1223–1223.
66 Rigaku Oxford Diffraction, CrysAlisPro software system, version 1.171.40.54, Rigaku Corporation, Oxford, 2019.
67 G. M. Sheldrick, *Found. Crystallogr.*, 2015, **71**, 3–8.
68 O. V. Dolomanov, L. J. Bourhis, R. J. Gildea, J. A. Howard and H. Puschmann, *Appl. Crystallogr.*, 2009, **42**, 339–341.
69 G. M. Sheldrick, *Cryst. Struct. Commun.*, 2015, **71**, 3–8.
70 M. Llunell, D. Casanova, J. Cirera and J. Bo, *SHAPE (Version 2.1)*, 2013.
71 K. Brandenburg and H. Putz, DIAMOND Version 3.2, Crystal Impact GbR, *Bonn, Germany*, 2009.
72 E. Bill, *julX_2S, Program for Simulation of Molecular Magnetic Data*, 2014.
73 F. Neese, *Wiley Interdiscip. Rev.:Comput. Mol. Sci.*, 2012, **2**, 73–78.
74 F. Weigend and R. Ahlrichs, *Phys. Chem. Chem. Phys.*, 2005, **7**, 3297–3305.
75 F. Weigend, *Phys. Chem. Chem. Phys.*, 2006, **8**, 1057–1065.
76 A. Hellweg, C. Hättig, S. Höfener and W. Klopper, *Theor. Chem. Acc.*, 2007, **117**, 587–597.
77 R. F. Bader, *Acc. Chem. Res.*, 1985, **18**, 9–15.
78 Y.-M. Chen, C.-Z. Wang, Q.-Y. Wu, J.-H. Lan, Z.-F. Chai, C.-M. Nie and W.-Q. Shi, *J. Mol. Liq.*, 2020, **299**, 112174.
79 (*a*) A. Patwal, R. Rana, G. Rajaraman and R. Murugavel, CCDC 2448658: Experimental Crystal Structure Determination, 2025, DOI: **10.5517/ccdc.csd.cc2n60zw**; (*b*) A. Patwal, R. Rana, G. Rajaraman and R. Murugavel, CCDC 2448659: Experimental Crystal Structure Determination, 2025, DOI: **10.5517/ccdc.csd.cc2n610y**; (*c*) A. Patwal, R. Rana, G. Rajaraman and R. Murugavel, CCDC 2448660: Experimental Crystal Structure Determination, 2025, DOI: **10.5517/ccdc.csd.cc2n611z**.